NeuroImage 181 (2018) 645–658

Contents lists available at ScienceDirect

NeuroImage

journal homepage: www.elsevier.com/locate/neuroimage

# Tractography optimization using quantitative T1 mapping in the human optic radiation

Roey Schurr[a,1], Yiran Duan[b,1], Anthony M. Norcia[b], Shumpei Ogawa[c,d], Jason D. Yeatman[e,f], Aviv A. Mezer[a,*]

[a] Edmond & Lily Safra Center for Brain Sciences, The Hebrew University of Jerusalem, Jerusalem, Israel
[b] Department of Psychology, Stanford University, CA, USA
[c] Department of Ophthalmology, Atsugi City Hospital, Kanagawa, Japan
[d] Department of Ophthalmology, The Jikei University School of Medicine, Tokyo, Japan
[e] Institute for Learning and Brain Sciences, University of Washington, Seattle, WA, USA
[f] Department of Speech & Hearing Sciences, University of Washington, Seattle, WA, USA

A R T I C L E I N F O

*Keywords:*
Tractography evaluation
Relaxometry
T1
Optic radiation

A B S T R A C T

Diffusion MRI tractography is essential for reconstructing white-matter projections in the living human brain. Yet tractography results miss some projections and falsely identify others. A challenging example is the optic radiation (OR) that connects the thalamus and the primary visual cortex. Here, we tested whether OR tractography can be optimized using quantitative T1 mapping. Based on histology, we proposed that myelin-sensitive T1 values along the OR should remain consistently low compared with adjacent white matter. We found that complementary information from the T1 map allows for increasing the specificity of the reconstructed OR tract by eliminating falsely identified projections. This T1-filtering outperforms other, diffusion-based tractography filters.

These results provide evidence that the smooth microstructural signature along the tract can be used as constructive input for tractography. Finally, we demonstrate that this approach can be applied in a case of multiple sclerosis, and generalized to the HCP-available MRI measurements. We conclude that multimodal MRI microstructural information can be used to eliminate spurious tractography results in the case of the OR.

## 1. Introduction

*In vivo* investigations of the human brain using MRI have advanced dramatically over the past two decades. This is particularly true for studying the long projections of the white matter using diffusion MRI. This technique is sensitive to local tissue architecture at the micrometer scale, including fiber orientation (Chenevert et al., 1990; Stejskal and Tanner, 1965). Tractography algorithms exploit this local signal to reconstruct 3D streamlines, representing the trajectory of white-matter pathways. Nearly all measurement methods are subject to a sensitivity-specificity tradeoff, and tractography is no exception: The tractography-derived streamlines either miss some of the underlying fascicles (false negatives), or include spurious streamlines that do not correspond to actual fascicles in the underlying tissue (false positives) (Knösche et al., 2015; Maier-Hein et al., 2017; Thomas et al., 2014). This limits the accurate mapping of white-matter tracts.

A good example for the challenges in tractography is the case of the optic radiation (OR). The human OR is a white-matter tract connecting the lateral geniculate nucleus (LGN) of the thalamus, to the primary visual area, V1. The OR is commonly used to demonstrate the performance of new tractography methods for both methodological and clinical reasons (Chamberland et al., 2016; Kammen et al., 2016; Lim et al., 2015; Portegies et al., 2015; Sherbondy et al., 2008b; Tournier et al., 2012). The challenges in tractography reconstruction, and in OR reconstruction in particular, have been attributed to a variety of factors. Importantly, the local diffusion signal is ambiguous – similar signals can arise from different fascicle configurations, such as crossing and kissing (Jbabdi and Johansen-Berg, 2011). This leads to local errors in the tractography tracking process, which can propagate and lead to unfavorable global effects in tractography. For example, a recent challenge based on a

*Abbreviations:* OR, optic radiation; T1-STD, T1 standard deviation; T1-Mdn, T1-median; ML, Meyer's loop; MS, Multiple sclerosis.

* Corresponding author. Edmond & Lily Safra Center for Brain Sciences, The Hebrew University of Jerusalem, Jerusalem, Israel.
*E-mail address:* aviv.mezer@elsc.huji.ac.il (A.A. Mezer).

[1] These authors contributed equally to this work.

https://doi.org/10.1016/j.neuroimage.2018.06.060
Received 25 January 2018; Received in revised form 3 June 2018; Accepted 20 June 2018
Available online 21 June 2018

simulated diffusion MRI dataset from the human brain showed that while state-of-the-art probabilistic tractography algorithms largely reduce the occurrence of false negative results, they produce a large number of false positive streamlines (Maier-Hein et al., 2017). Indeed, the same study found that the OR was one of the hardest tracts to identify accurately. This is particularly true of the challenging anterior sub-bundle of the OR, including Meyer's loop. Therefore, when tracking specific white-matter tracts, as in the case of the OR, multiple spatial landmarks are often used to minimize false positive results (Catani and Thiebaut de Schotten, 2008; Dayan et al., 2015; Kammen et al., 2016; Martínez-heras et al., 2015).

The field has introduced a plethora of new methods to mitigate the sensitivity-specificity tradeoff in tractography, each targeting a different step in the tractography pipeline (Wandell, 2016). These include advanced techniques for data acquisition (Frank, 2001; Tuch et al., 2003), sophisticated models of the local diffusion signal (Ozarslan et al., 2013; Rokem et al., 2015; Tournier et al., 2007; Tuch et al., 2003), global tractography algorithms and tractography evaluation techniques (Daducci et al., 2015; Pestilli et al., 2014; Sherbondy et al., 2008a; Smith et al., 2015). A recent advancement is microstructure-informed tractography, which aims to map microstructural properties along white-matter fascicles. These algorithms build on the assumption that the microstructural properties remain constant, or change smoothly, along the fascicle (Daducci et al., 2016; Alexander et al., 2017). While current microstructure-informed tractography algorithms use only diffusion MRI data, they can benefit greatly from multimodal MRI-based microstructural inputs. Indeed, it has been hypothesized that tractography analysis could be integrated with other MR imaging measurements to mitigate its current limitations (Alexander et al., 2017; Jbabdi and Johansen-Berg, 2011; Maier-Hein et al., 2017). This hypothesis can now be tested using quantitative MRI (qMRI) techniques, which provide complementary information about the white-matter microstructure.

The goal of the current study is to test the specific hypothesis that microstructural information derived from a quantitative T1 map can be used for evaluating tractography results of the human OR and differentiating valid streamlines from invalid ones. Postmortem studies have shown that the OR has consistently high myelination compared to adjacent white-matter tracts (Fig. 1b) (Bürgel et al., 1999). T1 is thought to be sensitive to myelination, where higher myelin content leads to lower T1 values (Lutti et al., 2014; Stüber et al., 2014). We found that the OR's smooth myelination signature is reflected in the T1 map (Fig. 1b–c; Supplementary Fig. 1). We propose that streamlines representing true OR fascicles have a relatively consistent microstructural signature along their path, which is indicated by a low-value T1 profile. Based on this T1-consistency finding, we developed a T1-filtering approach, in which information from a T1 map is integrated into the process of tractography evaluation of the OR, allowing the elimination of false positive results (Fig. 1d). We found that in the case of the OR, T1-filtering complements diffusion-based filters. We then show that tractography evaluation of the OR using T1 mapping can be applied in a case of focal white-matter lesions. Moreover, we generalize our approach to the myelin related semi-quantitative contrast of T2-weighted divided by T1-weighted images (Glasser and Van Essen, 2011).

## 2. Methods

### 2.1. Subjects

In this article we used two datasets, one from (Yeatman et al., 2014) and one from the Human Connectome Project (HCP; Van Essen et al., 2012).

The subjects of the first dataset were taken from a larger dataset collected at Stanford University (Yeatman et al., 2014). For this study, we selected a subset of subjects using the following criteria: right-handed adults between the ages of 18 and 55 years. Three of the subjects were excluded from this study as their anatomical scans did not include the entire occipital lobe. From the original 102 subjects, this yielded a selection of 31 subjects (14 men; mean $\pm$ STD age $33 \pm 11$ years). In addition, we included one volunteer with relapsing-remitting multiple sclerosis (male, age 42) from the same dataset.

Data collection procedures were approved by the Stanford University Institutional Review Board. Subjects were recruited from the San

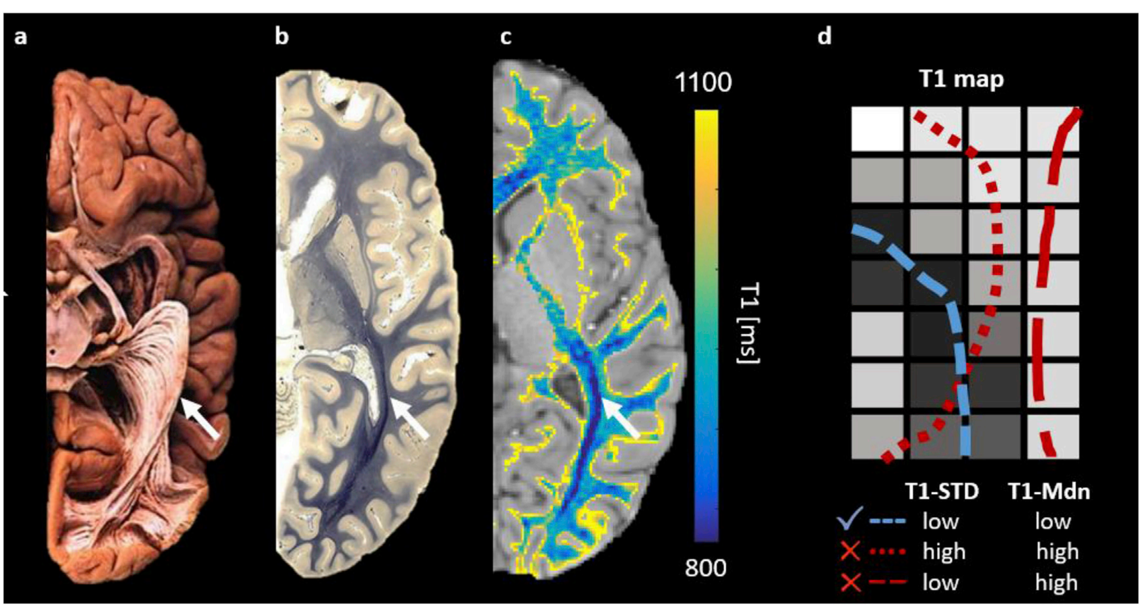


**Fig. 1. The optic radiation (OR) has a unique microstructural signature.** (**a**) The OR in a dissected postmortem brain shown from below. (**b**) In an axial slice of a brain stained for myelin the OR is seen to be highly myelinated (dark) compared to surrounding tissue. Credit to National Science Foundation. (**c**) A quantitative T1 map of the white matter overlaid on top of a T1-weighted image of the same subject. The OR has a unique signature of low T1 values compared to surrounding tissue. (**d**) A schematic illustration of the T1-consistency hypothesis: The T1 profiles along true OR streamlines from diffusion-MRI tractography should have low standard deviation (T1-STD) and low median values (T1-Mdn). Here only the light blue streamline truly corresponds to the OR. The image in (a) was reproduced from the Virtual Hospital (Williams et al., 1997). The image in (b) was kindly provided by the Brain Biodiversity Bank, Michigan State University (https://www.msu.edu/~brains/brains/human/index. html), which received funding from the U.S. National Science Foundation.

Francisco area and were screened for neurological, cognitive and psychiatric disorders. All subjects provided informed consent.

The second dataset included a subset of 30 unrelated randomly selected subjects (14 male) from the HCP dataset. All subjects are young adults at the age of 22–35.

### 2.2. MRI acquisition and processing

Data for the first dataset were collected at Stanford University's Center for Cognitive and Neurobiological Imaging (www.cni.stanford.edu), using a 3T General Electric Discovery 750 (General Electric Healthcare, Milwaukee, WI, USA) equipped with a 32-channel head coil (Nova Medical, Wilmington, MA, USA).

#### 2.2.1. T1 mapping

For the first dataset, T1 relaxation was computed from spoiled gradient (SPGR) echo images acquired at different flip angles ($\alpha = 4^\circ$, $10^\circ$, $20^\circ$, $30^\circ$, TR = 14 ms, TE = 2.4 ms) and spatial resolution of 1 $mm^3$ isotropic. The data contained an additional spin echo inversion recovery (SEIR) scan that is free from transmit-coil inhomogeneity (Barral et al., 2010; Mezer et al., 2013). The SEIR was done with an echo planar imaging (EPI) readout, a slab inversion pulse, and spectral spatial fat suppression. For the SEIR-EPI acquisition, the TR was 3 s; echo time was set to minimum full; inversion times were 50, 400, 1,200, and 2400 ms. The SEIR resolution is 2 $mm^2$ in-plane with a slice thickness of 4 mm. The EPI readout was performed using 2 × acceleration to minimize spatial distortions. Whole-brain T1 maps were computed as described in previous publications (Berman et al., 2017; Mezer et al., 2016, 2013). In short, unbiased T1 maps were calculated using the SPGRs which were corrected for B1 excite inhomogeneity using the unbiased SEIR data (Barral et al., 2010). For each subject, we also synthesized a T1-weighted (T1w) image from the multi flip-angle SPGR images. The analysis pipeline for producing the unbiased T1 maps is an open source MATLAB code available at (https://github.com/mezera/mrQ). We used ANTs to non-linearly warp the T1 map to the space of the diffusion MRI data.

In addition, for the multiple sclerosis patient, a fluid-attenuated inversion recovery (FLAIR) image was acquired with 0.43 × 0.43 mm in-plane resolution and 5 mm axial slice thickness.

#### 2.2.2. T2w divided by T1w contrast images

For the HCP dataset, we analyzed the structural MRI that included T1-weighted and T2-weighted images with 0.7 mm isotropic spatial resolution. First, we divided the T2-weighted and T1-weighted images to obtain a T2w/T1w image. The contrast of this image is similar to that of a quantitative T1 map, and opposite to contrast of the commonly used T1w/T2w image (Glasser and Van Essen, 2011). Taking the ratio of two images removes most of the shared biases, like the receive-coil inhomogeneities. Remaining slow-varying biases in space due to imperfections such as residual excite coil inhomogeneity were removed using the N4 algorithm in ANTs (Tustison et al., 2010) with a white-matter probability map as a weights mask input to the algorithm, to reduce partial volume effects (Tustison et al., 2014). Last, we used ANTs to non-linearly warp the T2w/T1w image to the space of the diffusion MRI data.

#### 2.2.3. Diffusion weighted imaging

Diffusion weighted MRI data for the first dataset were acquired using dual spin-echo diffusion-weighted sequences with full-brain coverage. Diffusion weighting gradients were applied at 96 non-collinear directions across the surface of a sphere as determined by the electrostatic repulsion algorithm (Jones et al., 1999). In all subjects, diffusion MRI data were acquired at 2 mm isotropic spatial resolution and the strength of the diffusion weighting was set to b = 2000 s/$mm^2$ (TE/TR = 93.60/7, 800 ms, G = 53 mT/m, $\delta$ = 21 ms, $\Delta$ = 25.4 ms). The data include eight non-diffusion-weighted images ($b = 0$) at the beginning of each measurement. Subject motion was corrected using a rigid-body alignment. Diffusion gradients were adjusted to account for the rotation applied to the measurements during motion correction. The dual spin-echo sequence we used does not require eddy current correction because it has a relatively long delay between the RF excitation pulse and image acquisition. This allows sufficient time for the eddy currents to dephase. Preprocessing was implemented in MATLAB (MathWorks, Natwick, MI, USA) and are publicly available as part of the Vistasoft GitHub repository (http://github.com/vistalab/vistasoft/mrDiffusion; see dtiInit.m).

For the HCP dataset we used high resolution HARDI data with b = 2000 s/mm2 and 90 diffusion directions with a spatial resolution of 1.25 mm isotropic spatial resolution (Feinberg et al., 2010; Moeller et al., 2010; Setsompop et al., 2012; Sotiropoulos et al., 2013).

### 2.3. Tractography of the OR

For each subject and hemisphere, we generated a set of 100,000 candidate OR streamlines confined to the white-matter mask using the probabilistic tractography algorithm implemented in ConTrack with default parameter values. In particular, we used dtiInit (Vistasoft) to identify the white-matter mask. To allow streamlines to enter the gray matter seed and target regions we define a relatively permissive stopping criterion (0.65 white-matter probability) for the ConTrack tracking algorithm. Seed and target regions of interest (ROIs) of thalamus and V1 were automatically extracted from the T1w image using FreeSurfer (Fischl, 2012). As these ROIs were defined in the SPGR space of the T1w images, we used ANTs (Avants et al., 2009) to warp them to diffusion MRI space. Specifically, we computed a non-linear transformation between the T1 map and the mean b0 image of the diffusion MRI data, minimizing the mutual information of the two volumes. Streamlines crossing the corpus callosum to the other hemisphere were discarded.

### 2.4. Automatic OR benchmark creation using spatial constraints

We developed an automated procedure for creating subject-specific OR bundles using spatial constraints. We refer to them as the "OR benchmark", as these bundles later served as the gold standard in assessing the performance of different tractography filtering methods. Following earlier work, the OR benchmark was defined as a subset of the 100,000 OR candidates, based on a series of spatial inclusion and exclusion criteria (See Appendix B). In short, only streamlines with endpoints at the lateral geniculate nucleus (LGN) were included. Streamlines entering the corpus callosum and streamlines going down through the pons were automatically discarded. To eliminate gross outliers, we discarded any streamlines whose length was more than 4 standard deviations above the mean fiber length. Finally, the resulting OR benchmarks were inspected by an expert neuro-ophthalmologist and manually edited if necessary.

### 2.5. Identifying white-matter tracts adjacent to the OR

We identified four fiber tracts adjacent to the OR in each individual hemisphere using the Mori atlas (Wakana et al., 2004) implemented in the Automated Fiber Quantification (AFQ) toolbox (Yeatman et al., 2012): Forceps Major (F. Major), Inferior Fronto-Occipital Fasciculus (IFOF), Inferior Longitudinal Fasciculus (ILF) and the Uncinate Fasciculus (UF) (see Fig. 2b). These fiber tracts were extracted from a whole-brain tractography performed using the MRtrix software (Tournier et al., 2012). We generated 500,000 streamlines confined to the white-matter mask using deterministic streamline tractography with default parameter values, and a maximum harmonic order ($l_{max}$) of 6.

### 2.6. Estimating T1 along white-matter tracts

Similar to the analysis in Yeatman et al. (2014), we used AFQ (Yeatman et al., 2012) to compute the T1 profile along the different tracts. In addition a similar analysis was done for the OR benchmarks.

Briefly, each streamline was resampled to 100 equally spaced nodes, and the T1 of each node was sampled from the warped T1 map. The tract core was calculated as the robust mean position of all streamlines per node. The T1 tract profile was calculated along the core of the tract as a weighted sum of the T1 values of all the streamlines at any given node, weighted by the Mahalanobis distance of each streamline from the core of the tract.

We additionally calculated the T1 profile separately for the anterior sub-bundle that includes the Meyer's loop of the OR. The anterior sub-bundle was defined by all OR benchmark streamlines that extended more than 8 mm anterior to the LGN.

### 2.7. Tractography filtering

#### 2.7.1. Tractography filtering using T1 mapping

The candidate set of OR streamlines included many false-positive streamlines. To obtain an optimized subset representing the OR, we filtered streamlines by setting an upper threshold on summary statistics derived from their T1 profiles. First, we computed the T1 profile of each streamline based on the subject's warped T1 map, using the AFQ (Yeatman et al., 2012). We next calculated the standard deviation and the median values of each streamline's T1 profile, which we refer to as T1-STD and T1-Mdn, respectively. Streamlines were then filtered out using one of three different methods: using an upper threshold on T1-STD, or on T1-Mdn, or on both T1-STD and T1-Mdn (T1-STD-Mdn filtering). We explored a range of thresholds, determined as percentiles of the full candidate set. For a single statistic, we used the following percentiles: 0.1, 0.5, 1, 2, 3, 5–95 in steps of 2, 97, 98, 99, 99.5, 99.9 and 100. For two combined statistics, we additionally used all possible pairs of these values for both statistics.

We compared our T1-filtering approach with two published methods for tractography filtering that are based on the fit to the diffusion MRI data: ConTrack scoring (Sherbondy et al., 2008a) and Linear Fascicle Evaluation (LiFE) (Caiafa and Pestilli, 2017).

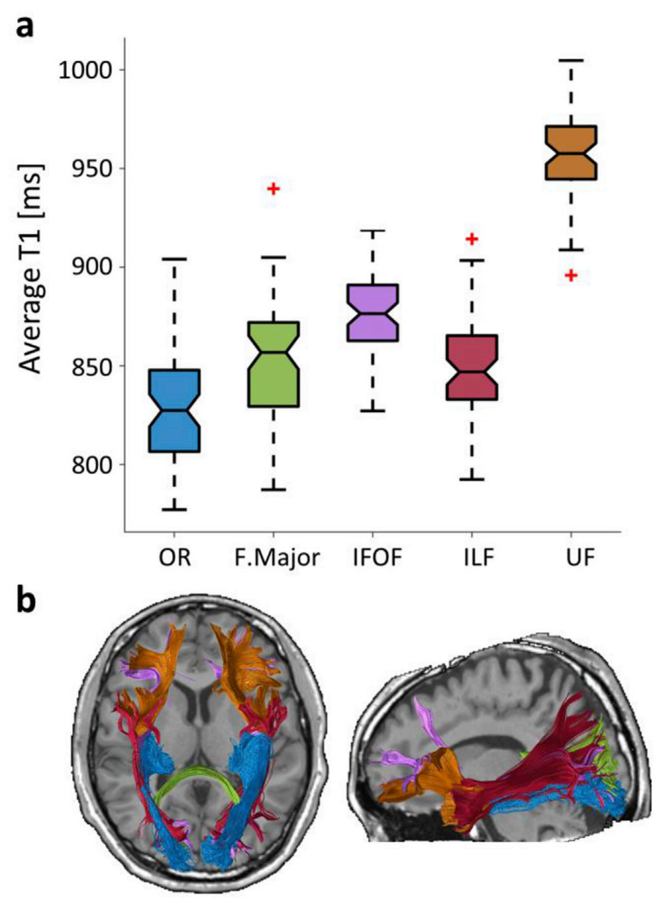


**Fig. 2. The distinct T1 signature of the OR.** (**a**) Boxplots indicating the average T1 along the core of the OR benchmark and adjacent white-matter tracts (averaged across $n = 62$ hemispheres). The OR benchmark shows the lowest T1 on average. Center lines indicate median values; notch indicates 95% confidence interval for the median; box limits indicate the interquartile range (IQR; 25$^{th}$-75th percentiles); whiskers extend to the most extreme data points within $1.5 \times$ IQR outside the box; outliers are represented as red crosses. The OR T1 is significantly lower compared with other tracts (paired samples *t*-test with Bonferroni correction ($p < 2 \times 10^{-8}$ for all tracts). (**b**) Axial and sagittal views of the reconstructed white-matter tracts overlaid on a T1-weighted image in one representative subject (OR, blue; F. Major, green; IFOF, purple; ILF, red; UF, brown).

#### 2.7.2. Tractography filtering using ConTrack scoring

The ConTrack scoring algorithm assigns each streamline a score that combines the fit of local streamline orientation to the local diffusion data, as well as prior information regarding the streamline length and smoothness (Sherbondy et al., 2008a). For all subjects, we explored a range of ConTrack scores, using the same percentile values as above.

#### 2.7.3. Tractography filtering using LiFE

While ConTrack was designed for tracking between two predefined ROIs, the LiFE algorithm for tractography filtering requires as input a set of whole-brain streamlines (i.e., a tractogram). We therefore generated for each subject a whole brain tractogram similarly to Section 2.5, but with the probabilistic streamline method (SD_PROB). We combined the resulting tractogram with the 200,000 OR candidates generated using ConTrack. LiFE optimizes a set of streamlines by keeping only those streamlines which are necessary to predict the original diffusion data. Each streamline is assigned a weight which reflects its contribution to that prediction (Caiafa and Pestilli, 2017; Pestilli et al., 2014). The whole-brain optimized tractogram is obtained by keeping only streamlines with a nonzero weight. To obtain the subset of optimized streamlines corresponding to the OR and to account for differences in the stopping criteria of the two tractography methods, we only kept those streamlines whose endpoints are within 4 mm from the thalamus and V1 ROIs.

#### 2.7.4. Tractography filtering assessment using ROC curves

To quantitatively assess the accuracy of each tractography filtering method, we used a receiver operator characteristic (ROC) analysis similar to that used in previous studies (Clatworthy et al., 2010; Lim et al., 2015; Thomas et al., 2014). This method is based on the voxelwise overlap between the filtered subset and some ground truth. We used the benchmark OR as the gold standard to identify whether the OR passes through each voxel. We evaluated each filtered subset by determining which voxels in the filtered subset are within the benchmark OR (hit) and which are not (false alarm). For each set of streamlines (candidate set, T1-filtered subset using a specific threshold etc.), we computed a binary image that represent all voxels with at least one streamline passing through it. We denote the binary images of (1) the candidate set, (2) the benchmark subset and (3) the filtered subset as $M_{can}$, $M_{ben}$ and $M_{fil}$, respectively. For each filtered subset of streamlines we defined the true positive rate (TPR, also known as sensitivity, or 'hit') as the fraction of $M_{fil}$ voxels that are shared with $M_{ben}$. We defined the false positive rate (FPR, equal to 1-specificity, also known as false alarm) as the fraction of $M_{fil}$ voxels that are shared with $M_{can}$ but not with $M_{ben}$:

$$sensitivity = TPR = \frac{\sum (M_{fil} \& M_{ben})}{\sum (M_{fil})}$$

$$1 - specificity = FPR = \frac{\sum [M_{fil} \& \ (!M_{ben})]}{\sum [(M_{can}) \& (!M_{ben})]}$$

where the sum is over all voxels in the map and "!" denotes the logical

NOT operator.

Using the calculated sensitivity and specificity values, each filtered subset is represented as a point in the sensitivity versus 1-specificity plane. By varying the filtering threshold value (e.g., maximal T1-STD), a full ROC curve can be plotted. For the case of combined T1-STD and T1-Mdn thresholds, we created a single curve by progressing from (1-specificity) = 0 to (1-specificity) = 1, including only points whose sensitivity is higher or equal to all previous points.

In the case of LiFE-filtering, no threshold was used, and each subject had only one subset of streamlines (all those that were assigned a non-zero weight). LiFE results for each hemisphere were therefore represented as a single point in the sensitivity versus 1-specificity plane.

To plot the mean ROC curve for each method across subjects and hemispheres, we represented each curve using a smoothing spline, which we then sampled in 100 equally distant points between 0 and 1. The best ROC curve is the one that passes closest to the optimal point of the upper left corner, where perfect sensitivity and specificity are obtained (Fig. 6a).

To evaluate the ROC curves of each method quantitatively, we computed two commonly used summary statistics, the area under the curve (AUC) of the ROC curve, and the maximal Youden's index along the curve, $J_{max}$ (Youden, 1950). The AUC is often used to measure how well a classifier discriminates between two classes, in this case between false-positive and true-positive voxels. Youden's index (J) is a point-wise measure of the ROC curve, defined as:

$J = \text{sensitivity} + \text{specificity} - 1$, and ranges between $-1$ and 1. To obtain high J, both sensitivity and specificity must be high. A greater weight can be given to either sensitivity or specificity by defining a weighted Youden's index (wJ) with $0 \le w \le 1$:

$$wJ = (1\text{-}w)\cdot\text{sensitivity} + (1+w)\cdot\text{specificity} - 1.$$

#### 2.7.5. Disentangling intra-white matter and inter-tissue effects in T1-filtering

To test whether T1-filtering also removes false-positive candidates that remain strictly within the white matter, or only those that traverse the subcortical gray matter, we repeated the T1-filtering analysis, this time removing any non-white matter voxels before calculating the T1 profiles. For this aim, white-matter voxels were defined using the FreeSurfer white-matter mask, warped to diffusion space. See Supplementary Text for a detailed description of this analysis.

#### 2.7.6. T2w/T1w-filtering

The subsequent analysis pipeline of the HCP data was identical to that used for the first dataset above, except that a T2w/T1w contrast image was used instead of a quantitative T1 map.

#### 2.7.7. T1-filtering in the presence of focal lesions

To test whether T1-filtering can be used in the presence of focal white-matter lesions, we tested the method on a patient suffering from multiple sclerosis. In this patient brain, the white-matter lesions were automatically identified using FreeSurfer as hypointensities in the T1w image. These were used to create a lesion mask, which was manually edited based on the FLAIR image.

The T1-filtering pipeline for the patient was identical to that used for the first dataset, with two changes. First, the white-matter mask used for tractography included the lesioned regions as determined in the lesion mask. Second, when calculating T1 profiles of the streamlines for T1-filtering, we ignored voxels included in the lesion mask.

### 2.8. Anatomical measurements

To measure the distance between Meyer's loop and the temporal pole (ML-TP), we segmented the temporal pole using FreeSurfer and non-linearly warped it to the space of diffusion MRI data using ANTs. We manually identified the most anterior point in Meyer's loop in both the OR benchmark and the T1-filtered OR. The ML-TP distance was calculated as the difference in the y-coordinate (anterior-posterior axis) between Meyer's loop and the most anterior point of the temporal pole ROI as in (Lilja and Nilsson, 2015).

### 2.9. Code availability

All code for OR benchmarks creation and OR T1-filtering is publicly available as open source Matlab code in GitHub https://github.com/MezerLab/T1-filtering-OR.

## 3. Results

### 3.1. The OR has a distinct T1 signature

The OR is a highly myelinated white-matter pathway that can be identified in postmortem brains using myelin staining (Fig. 1b; Bürgel et al., 1999). T1 was shown to be highly sensitive to myelin content in white matter. Indeed, the OR is readily identified in all subjects in our data by a signature of low T1 values in multiple slices (Fig. 1c, Supplementary Fig. 1).

To quantify the difference between the T1 of the OR and adjacent white-matter tracts, we identified subject-specific OR bundles using spatial inclusion and exclusion criteria (see Appendix B) that were validated by an expert neuro-ophthalmologist. The adjacent white-matter tracts were automatically identified using the Mori atlas (Wakana et al., 2004; Yeatman et al., 2012). We found that the mean T1 along the core of the OR (mean ± STD $831 \pm 30$ ms) is significantly lower compared with other white-matter tracts (F. Major: $853 \pm 33$ ms, IFOF: $877 \pm 25$ ms, ILF: $850 \pm 26$ ms, UF: $957 \pm 21$ ms; Fig. 2). These differences are statistically significant in a paired samples *t*-test with Bonferroni correction ($p < 2 \times 10^{-8}$ for all tracts). This includes both tracts that follow the OR for a portion of its course (e.g., the IFOF and the ILF; Goga and Türe, 2015), as well as tracts that cross in the vicinity of the OR (e.g., the UF; Kier et al., 2004).

### 3.2. The OR T1 profile in space

The typical T1 profile of the OR across the population shows lower T1 values (Fig. 3) compared with adjacent white-matter tracts (Supplementary Fig. 2). This is particularly evident for the UF. Similarly, segments of the ILF and IFOF have T1 values that are higher compared with the OR. At their posterior segments, however, as they share their course with the OR (and the IFOF adjoins the OR to form the Sagittal Stratum (Catani et al., 2003)), their T1 values are naturally very close to those of the OR as they sample similar voxels. In addition, we calculated the T1 profile of the anterior sub-bundle of the OR, which includes Meyer's loop. While the most anterior region showed relatively higher T1 values then the full OR, it is still very close to the typical T1 of the entire OR (Fig. 3a, inset).

### 3.3. Tractography filtering using T1 mapping

To test the hypothesis that quantitative T1 can provide useful microstructural information for tractography optimization of the human OR, we used the T1 map to differentiate between valid (true positive) and invalid (false positive) streamlines in 62 hemispheres (Figs. 4–6). Fig. 5a shows the initial candidate set of the OR streamline tracked between thalamus and V1. As expected, this candidate set suffers from low specificity and includes many false positive streamlines that deviate from the true OR path, since minimal anatomical landmarks used for tractography seeding (Benjamin et al., 2014; Martínez-heras et al., 2015).

The histology-based hypothesis predicts that true OR streamlines have a consistent microstructural signature of low T1 values along their path (high myelin, Fig. 1d, Supplementary Fig. 1). When plotting all

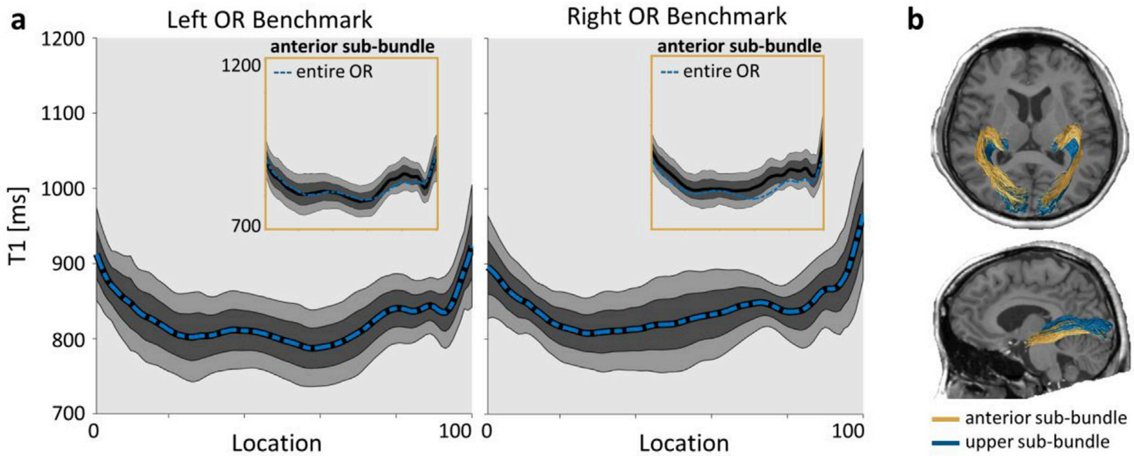


**Fig. 3. T1 profile along the OR.** (**a**) The dashed blue curves shows the mean T1 profile of the OR across the population (n = 31 subjects), progressing from posterior to anterior (0–100), for the left and right hemispheres. The dark and light gray regions indicate the 25th-75th percentiles and $10^{th}$-$90^{th}$ percentiles, respectively. Insets show the T1 profiles of the anterior sub-bundle of the OR (y-axis scaled down). Here, the black curve indicates the mean profile, and the dashed blue curve is the corresponding mean profile of the entire OR, for reference. (**b**) An example subject showing the OR benchmark separated to its upper and anterior sub-bundles (see Methods).

candidate streamlines on the plane of median T1 (T1-Mdn) versus T1 standard deviation (T1-STD), we find great variability across streamlines (Fig. 4a and Supplementary Fig. 3). Importantly, we find that the benchmark OR streamlines (although constructed based purely on spatial inclusion and exclusion criteria) are clustered at the bottom left corner of this plane, indicating that they are characterized by low T1-Mdn and T1-STD compared with the other, false-positive, candidate streamlines. Furthermore the streamlines of other white-matter tracts, identified by the Mori atlas (see Methods), are clustered at different positions in this plane (Fig. 4b and Supplementary Fig. 4). This suggests that T1-Mdn and T1-STD can serve to identify the true OR from false positive candidate streamlines that “jump” to nearby pathways.

Next, we incorporated the histology-based OR T1 filter. Fig. 5 illustrates the T1-filtering process for one subject, in which we excluded streamlines with either a highly variable T1 profile (high T1-STD) or with a high value of median T1 along their path (high T1-Mdn). See Supplementary Figs. 5-9 for the T1-filtering process in additional subjects. The optimized set of streamlines appears to agree with the known neuroanatomy of the OR. Importantly, it includes the OR's most anterior part, Meyer's loop, in 61 of 62 hemispheres (see additional examples in Supplementary Figs. 5-9). Supplementary Fig. 7 shows the single unusual hemisphere. We note that choosing a different pair of thresholds allows the preservation of Meyer's loop in that case as well. Visual inspection of Fig. 5 and Supplementary Figs. 5-9 verifies that the T1-filtering method allows the elimination of several groups of false-positive streamlines. Still, for this choice of filtering thresholds (T1-Mdn and T1-STD), some false-positive streamlines persist, most commonly around the thalamus.

The complementary nature of using both T1-STD and T1-Mdn for tractography filtering of the OR can be appreciated in Fig. 5b–c. We find that when filtering by T1-STD exclusively, some false-positive streamlines persist (Fig. 5b), which can be further eliminated by setting an upper threshold on T1-Mdn (Fig. 5e, Supplementary Figs. 5-9).

### 3.4. Sensitivity-specificity tradeoff across different filtering approaches

Next, we studied the sensitivity-specificity tradeoff of the T1-filtering approach, and compared it with other filtering techniques (Caiafa and Pestilli, 2017; Sherbondy et al., 2008a). We quantify it at the group level using a receiver operator characteristic (ROC) curve analysis. In calculating the sensitivity and specificity values, we used an anatomically-based OR benchmark as a subject-specific gold standard. The ROC curve is constructed by varying the filtering threshold: each threshold results in a different subset of streamlines, whose sensitivity and specificity values correspond to a particular point in the ROC curve. Fig. 6a illustrates two hypothetical schematic ROC curves. A good filtering method is one whose ROC curve passes close to the optimal point at the top left corner. Its area under the curve (AUC) and maximal Youden index along the curve, $J_{max}$, would be that which is closest to their maximal possible values of 1.

The proposed T1-filtering technique (Fig. 5) requires two user-specified thresholds (on T1-STD and T1-Mdn), expressed as percentiles across streamlines (see Methods). In Fig. 6 we plot the result of an extensive search in this parameter space for each subject. We plot the mean smoothed ROC curves across all 62 hemispheres using three tractography filtering methods based on a quantitative T1 map (T1-Mdn, T1-STD and the two filters together; see Supplementary Fig. 10 for ROC curves of all the individual subjects in this dataset). The performance of T1-STD-filtering and T1-Mdn-filtering is very similar in terms of specificity and sensitivity as indicated by their similar ROC curves. Both curves exceed 0.8 sensitivity at the cost of approximately 0.2 loss in specificity. The best results are obtained using a combined filtering approach based on both T1-STD and T1-Mdn. The combined T1-filtering outperforms T1-STD-filtering and T1-Mdn-filtering in terms of both AUC (mean ± STD $0.93 \pm 0.02$ compared to $0.88 \pm 0.05$ and $0.86 \pm 0.03$ respectively) and $J_{max}$ ($0.73 \pm 0.06$ compared to $0.65 + 0.09$ and $0.58 \pm 0.07$ respectively). These differences are statistically significant in a paired samples *t*-test with Bonferroni correction for both AUC (T1-STD-filtering: $t_{61} = 10$ $p = 2.1 \times 10^{-14}$; T1-Mdn-filtering: $t_{61} = 17.4$ $p = 2.7 \times 10^{-25}$, n = 62 hemispheres) and $J_{max}$ (T1-STD-filtering: $t_{61} = 9.1$ $p = 5.9 \times 10^{-13}$; T1-Mdn-filtering: $t_{61} = 19$ $p = 2.6 \times 10^{-27}$, n = 62 hemispheres). These results indicate that the T1 map holds valuable information that is useful for minimizing the sensitivity-specificity tradeoff in tractography of the human OR.

Next, we tested the possibility of using a single fixed pair of thresholds (percentiles) common to all subjects. For this analysis we selected the pair of thresholds that gave the greatest $J_{max}$ on average across subjects ([35, 67] percentiles for T1-STD and T1-Mdn respectively). We found that these fixed thresholds gave an average $J_{max}$ of 0.64. Compared with the extensive search for an optimal pair of thresholds per subject, the fixed thresholds common to all subjects lead to an average decrease of only 0.09 in $J_{max}$. Based on a qualitative subjective assessment of the T1-filtered streamlines, we found that maximizing the weighted J values (wJ) with w = 0.3 is advantageous, as it eliminates more false-positive streamlines while preserving the expected shape of the OR, even

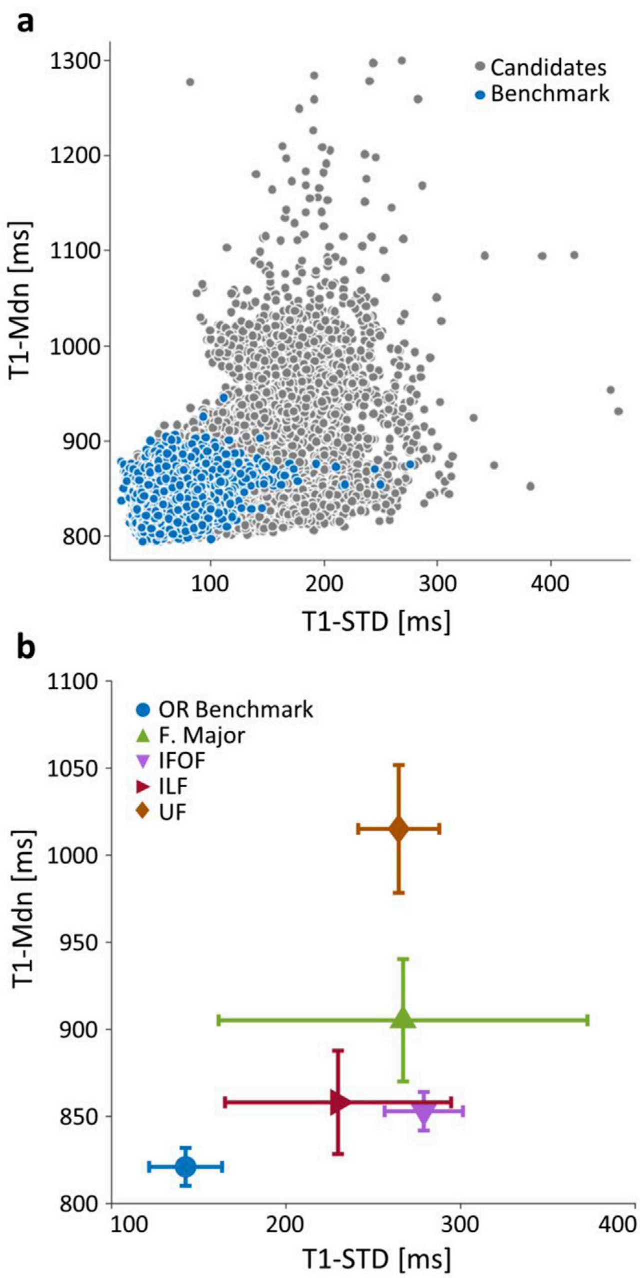


**Fig. 4. T1-STD and T1-Mdn of the OR and adjacent tracts.** (**a**) T1-STD and T1-Mdn of the OR candidate streamlines and the OR benchmark. Circles marks the positions of each streamline in the plane of T1-STD and T1-Mdn for one representative subject. As expected by the myelin-based hypothesis for the T1 signature of the OR, streamline of the OR benchmark (blue) are generally characterized by low values of T1-STD and T1-Mdn compared with the rest of the candidate streamlines (gray). (**b**) The typical T1-STD and T1-Mdn of the OR benchmark and adjacent white-matter tracts. Data represented as mean ± STD per axis. See all subjects in Supplementary Figs. 3-4.

though its false negative rate is naturally increased compared with $J_{max}$ (Fig. 5; Supplementary Figs. 5-9).

Last, the distances between Meyer's loop and the temporal pole (ML-TP) were very similar for the benchmark OR (27.4 ± 3.6 mm) and the T1-filtered OR (27.4 ± 3.4 mm). No significant difference was found in a paired samples *t*-test ($t_{61} = 0.05$ $p = 0.96$, $n = 62$ hemispheres). These values also agree with previous literature based on postmortem dissections (Ebeling and Reulen, 1988; Lilja et al., 2014).

### 3.5. Comparing T1-filtering with diffusion-based tractography filtering

We compared the T1-filtering approach with tractography filtering based on the diffusion MRI signal. First, we applied the ConTrack scoring algorithm commonly used for tractography filtering of the OR. In ConTrack, a streamline is assigned a high score if its local orientation fits well the diffusion data, and if it complies with prior assumptions regarding streamline length and smoothness. The ROC curves in Fig. 6b show that the information extracted from the T1 map is complementary to the diffusion data used by ConTrack's diffusion-filtering. The mean ROC curve across all hemispheres for the combined T1-filtering approach is closer to optimal compared with ConTrack's mean ROC curve (Fig. 6c–d). This discrepancy between T1-filtering and ConTrack is further quantified by the statistically significant difference in AUC (mean ± STD $0.93 \pm 0.02$ and $0.75 \pm 0.05$ respectively; $t_{61} = 24$ $p = 8.9 \times 10^{-33}$, paired samples *t*-test with Bonferroni correction, $n = 62$ hemispheres) and $J_{max}$ ($0.73 \pm 0.06$ and $0.38 \pm 0.08$ respectively; $t_{61} = 25$ $p = 6.9 \times 10^{-34}$).

Then we compared the T1-filtering method with a state-of-the-art global tractography method based on diffusion MRI data, implemented by the linear fascicle evaluation (LiFE) algorithm (Pestilli et al., 2014). As expected, the LiFE-optimized tractogram included 10 ± 1% (mean + STD) of the streamlines in the input tractogram. LiFE successfully eliminated many of the false-positive streamlines (see Supplementary Fig. 11), but it also eliminated many streamlines considered as true OR streamlines according to our benchmark, leaving a sparse representation of the full tract. To visualize the sensitivity-specificity tradeoff in the LiFE-filtering optimized results, each hemisphere is shown as a separate point in the plane of sensitivity versus 1-specificity (Fig. 6b). We found an advantage of T1-filtering over LiFE-filtering for the OR, with a significant difference in $J_{max}$ ($0.73 \pm 0.06$ and $0.24 \pm 0.06$ respectively).

### 3.6. Disentangling intra-white matter and inter-tissue effects in T1-filtering

It was previously highlighted that including subcortical regions in the tractography propagation mask is essential to fully reconstruct the white-matter pathways (Girard et al., 2014; Li et al., 2012; Smith et al., 2012). While this increases the sensitivity of tractography results by reducing the occurrence of false-negative streamlines, it also introduces false-positive streamlines that traverse subcortical gray matter. We thus tested whether T1-filtering also removes false-positive candidates that remain strictly within the white matter, and not only those that traverse the subcortical gray matter. In the Supplementary Text and Supplementary Fig. 12 we show that indeed, T1-filtering eliminates both types of false-positive streamlines.

To conclude, our results indicate that integrating information from the T1 profiles of candidate OR streamlines can be used to differentiate between false positive and true positive results. By filtering the candidate set using two profile statistics, T1-STD and T1-Mdn, one can obtain an optimized OR streamline subset with high sensitivity while retaining a high level of specificity.

### 3.7. Generalizing tractography filtering using semi-quantitative MR images

We tested whether the OR T1-filtering approach could be generalized to non-quantitative weighted MRI, which is more widely used. Here we used a T2w/T1w image that was proposed to be sensitive to myelin content (Glasser and Van Essen, 2011). In this contrast image, as in the quantitative T1 map, the OR stands out as a dark region where expected (Fig. 7a).

Visual inspection of the filtered subset indicates that the STD and median values of the T2w/T1w profile are useful for filtering the candidate OR streamlines (Fig. 7a). An ROC curve analysis comparing T2w/T1w-filtering with the diffusion-based ConTrack filtering, shows that a better sensitivity-specificity tradeoff is achieved by the T2w/T1w-filtering (Fig. 7b). A significant difference between the T2w/T1w-

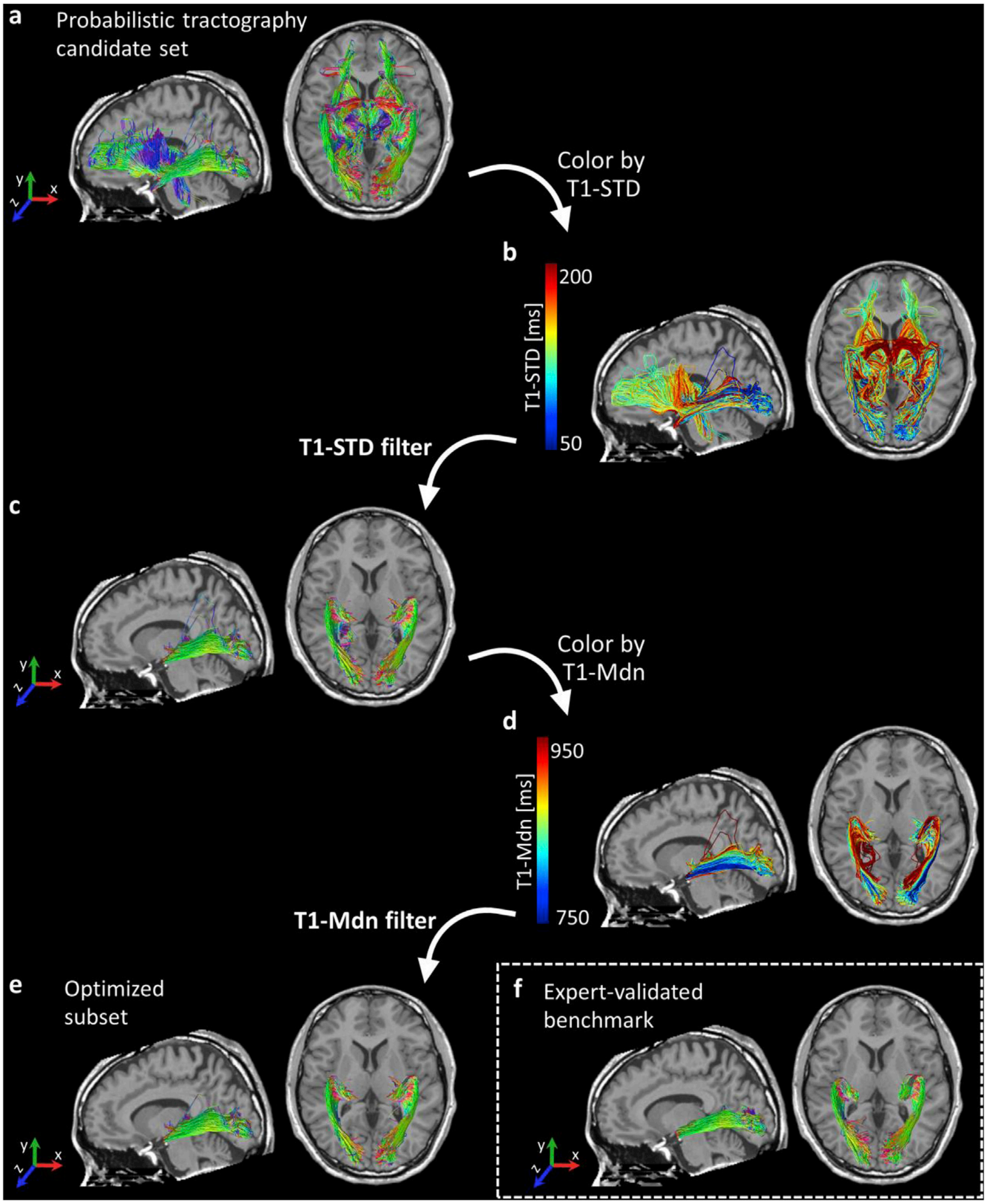


**Fig. 5. T1-filtering of the optic radiation (OR) in one subject.** (**a**) The candidate set of streamlines connecting the thalamus with area V1 includes many spurious streamlines. When colored by their T1-STD values (**b**), it is evident that many spurious streamlines have high T1-STD values. (**c**) The remaining subset of streamlines (in this example, thresholds were chosen by maximizing the wJ value in the ROC analysis, with w = 0.3; See Methods and Fig. 6). Many spurious streamlines have been eliminated. When colored by their T1-Mdn values (**d**), some spurious streamlines with high T1-Mdn values are apparent. (**e**) The final T1-filtered subset clearly resembles the benchmark OR in this subject, shown in panel (**f**). See additional subjects in Supplementary Figs. 5-9.

filtering and ConTrack-filtering was found also in terms of AUC of the ROC curve ($0.84 \pm 0.04$ and $0.77 \pm 0.05$ respectively; $t_{59} = 8.2$ $p = 2.4 \times 10^{-11}$, paired samples *t*-test, n = 60 hemispheres), and $J_{max}$ values ($0.54 \pm 0.09$, $0.42 + 0.08$- respectively; $t_{59} = 9.0$ $p = 1.2 \times 10^{-12}$, paired samples *t*-test, n = 60 hemispheres). These results verify that conventional, non-quantitative MR images that are sensitive to myelin content, such as T2w/T1w images, can be used for tractography filtering of the human OR. We note that the benefit of using T2w/T1w-filtering over the diffusion-based ConTrack-filtering was smaller than in the case of fully quantitative T1 mapping.

### 3.8. *T1-filtering in the presence of focal lesions (MS)*

We tested whether T1-filtering can be done on a subject presenting focal lesions due to multiple sclerosis. A lesion in the OR can be clearly seen in the subject's T1w image, as well as in the T1 profile along the core of the OR benchmark (Fig. 8a–b). The T1 profile outside the lesioned area falls within the population norm. Fig. 8c shows that by ignoring the lesioned voxels, we were able to use T1-filtering and obtain an optimized subset of streamlines that represent the OR, even in the presence of focal lesions.

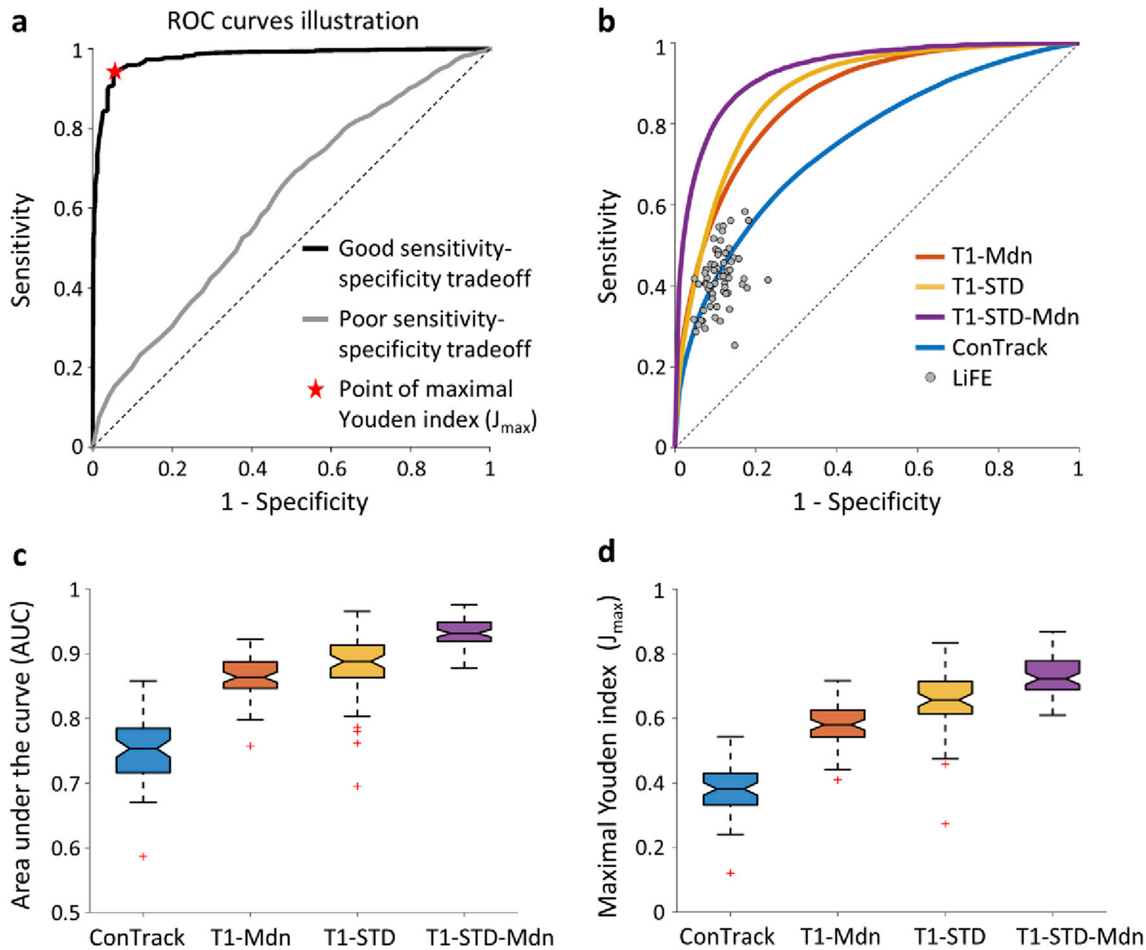


**Fig. 6. ROC analysis of the different filtering techniques in the OR.** (**a**) Illustration of two hypothetical ROC curves. Each curve represents one classification method, and each point along the curve represents the sensitivity and specificity given a specific threshold. The gray curve is characterized by poor sensitivity-specificity tradeoff. The black curve reaches close to the top left point, where maximal sensitivity and specificity are obtained. The red star marks the point of maximal Youden index ($J_{max} = 0.89$) for that curve. (**b**) The mean ROC curves (across 62 hemispheres) calculated voxelwise for each method. The combined T1-filtering uses both the standard deviation and median T1 along streamlines (T1-STD-Mdn, purple) and reaches closest to the optimal point, indicating that the T1 map holds valuable information for tractography filtering of the OR. Filtering only by the streamlines' median T1 values (T1-Mdn, orange) or only by their T1 standard deviation (T1-STD, yellow) gave suboptimal results. The diffusion-based filtering approach (ConTrack (Sherbondy et al., 2008a), blue) reached lower values. Gray circles represent the streamlines subsets obtained with LiFE (Pestilli et al., 2014), a diffusion-based global filtering approach. (**c-d**) Boxplots indicating the area under the curve (AUC) and the maximal Youden index ($J_{max}$) obtained by each tractography filtering method. Center lines indicate median values; notch indicates 95% confidence interval for the median; box limits indicate the interquartile range (IQR); whiskers extend to the most extreme data points within 1.5 × IQR outside the box; outliers are represented as red crosses; n = 62 sample points. In both summary statistics shown in panels (c) and (d), the combined T1-filtering technique (purple) obtains the highest values. See ROC curves of individual subjects in Supplementary Fig. 10.

## 4. Discussion

In this study, we provide substantial evidence for the recently proposed hypothesis that multi-modal MRI can help resolve the ambiguities that challenge current tractography algorithms (Jbabdi and Johansen-Berg, 2011; Maier-Hein et al., 2017; Wandell, 2016). Specifically, we introduce a tractography filtering framework that integrates quantitative T1 mapping to optimize the tractography results of the human optic radiation (OR). We show that the consistency in T1, which is sensitive to myelin content, is highly valuable for complementing the geometrical information extracted from diffusion MRI of the OR. We found that the T1-filtering outperforms two diffusion-based filtering approaches for the OR. The false-positive streamlines produced by diffusion MRI tractography of the OR can be eliminated based on their myelin sensitive T1 profile, thereby increasing tractography's specificity, while maintaining a high level of sensitivity.

In particular, these results also support the assumption of spatial smoothness of microstructural properties along white-matter fascicles, which is often implicitly made by microstructure informed tractography algorithms (Daducci et al., 2016).

Accurate *in vivo* delineation of the OR has important clinical implications. Tracking the OR has great importance for presurgical planning in neurological resections of the anterior temporal lobe, in which avoiding damage to the OR is essential for fully preserving the patient's visual field (Ebeling and Reulen, 1988; Sarubbo et al., 2015; Winston et al., 2014; Yogarajah et al., 2009). As an indispensable signal-relaying station in the human visual system, the OR is frequently implicated in a variety of diseases, such as multiple sclerosis (Reich et al., 2009), cerebral palsy (Hoon et al., 2009; Rushe et al., 2010), glaucoma (Kaushik et al., 2014), amblyopia (Duan et al., 2015; Xie et al., 2007) and others (Ogawa et al., 2014). Different tractography algorithms can yield different results (Bastiani et al., 2012; Jbabdi et al., 2015; Takemura et al., 2016), often characterized by a sensitivity-specificity tradeoff: while probabilistic tractography algorithms allow tracking more valid streamlines (increasing the sensitivity), this often comes at the cost of identifying more invalid streamlines (decreasing the specificity) (Zalesky et al., 2016). This tradeoff can be traced back to the ambiguity of the underlying diffusion signal (Mangin et al., 2002; Thomas et al., 2014). For example, Meyer's loop, the highly angulated anterior

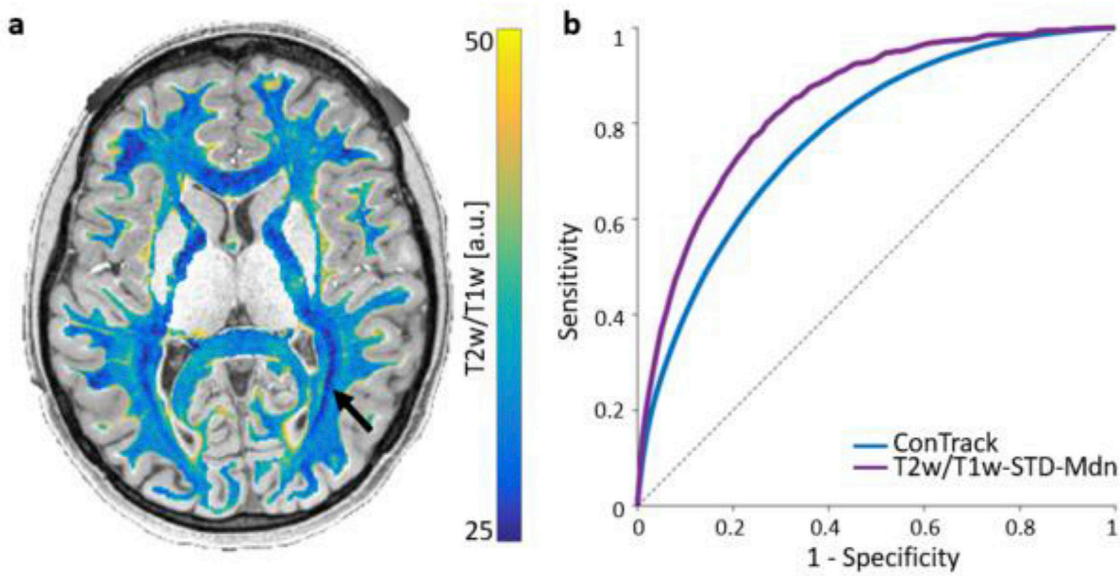


**Fig. 7. Tractography filtering using a T2w/T1w image in the HCP dataset.** (**a**) A T2w/T1w image of the white matter overlaid on top of a T1w image. As in the case of a quantitative T1 map, the highly myelinated OR has a unique signature compared to surrounding tissue (black arrow; compare with Fig. 1c). (**b**) The mean ROC curves (n = 60 hemispheres) obtained by the combined T2w/T1w-filtering (purple), and by the ConTrack diffusion-based filtering (blue). There is added value in using the semi-quantitative T2w/T1w image over using the diffusion data alone.

portion of the OR, is a bottleneck for tractography (Maier-Hein et al., 2017). In this region, the tractography algorithm generates spurious streamlines that "jump" between disparate white-matter tracts. Previous studies eliminated such spurious streamlines by incorporating spatial and anatomical constraints (Benjamin et al., 2014; Dayan et al., 2015; Martínez-heras et al., 2015; Portegies et al., 2015; Renauld et al., 2016; Stieglitz et al., 2011). In postmortem studies, the OR is identified by its consistently high myelin content (Bürgel et al., 2006, 1999; Ferguson, 1905). We have shown that this myelin signature is reflected by consistently low values in a quantitative T1 map (Fig. 1c; Supplementary Fig. 1), which differ from adjacent white matter. Based on these observations, we developed an *in vivo* myelin-based T1-filtering technique, and showed that the spatially consistent microstructural signature of the OR fascicles can serve as a regularization criterion for tractography, thereby eliminating most of the false positive streamlines. We found that T1-filtering can eliminate both intra-white matter and inter-tissue false-positive streamlines. We further demonstrated its application in the presence of focal white-matter lesions (Fig. 8). Like all tractography filtering methods, T1-filtering can only eliminate existing streamlines, but not create new ones. Therefore, the candidate set of streamline must cover the full extent of the reconstructed tract (e.g., Meyer's loop). Eliminating the false positives is particularly important for probabilistic tractography algorithms, which are designed to provide minimal false-negative results (Thomas et al., 2014; Zalesky et al., 2016). To the best of our knowledge, the present work is the first to use the streamlines T1 profiles for tractography evaluation and optimization (Fig. 5; Supplementary Figs. 5-9).

While the proposed T1-filtering method works well for the OR, it is probably not immediately applicable to other white-matter tracts, since the OR presents a unique case of pronounced difference in myelin content compared with other white-matter tracts. Generalizing such multi-modal microstructure informed tractography to whole-brain mapping will likely require a global optimization approach, where the full tractogram is used to simultaneously account for multiple microstructural measures along the tractography streamlines (Caiafa and Pestilli, 2017; Daducci et al., 2015). Developing such a global multi-modal approach could open new avenues in the characterization of white matter in the human brain. Furthermore, while we have demonstrated successful application of T1-filtering in a case of focal white-matter lesions, it is likely to fail in the clinical cases of diffuse lesions which affect the T1 signature throughout the OR. In this work we have not tested if the filtering algorithm performs similarly for T2w/T1w in the presence of white-matter lesions. It remains to be tested how T1-filtering of the OR performs for different age groups, since the T1 signatures of different white-matter pathways are known to change during the course of normal development and aging (Yeatman et al., 2014). A limitation of any *in vivo* study of the OR is the lack of ground truth delineation of the pathway. Here we developed an automatic procedure based on known anatomical landmarks to identify a gold standard OR. While we have found no significant difference in the ML-TP distance between the OR benchmark and the T1-fltered OR, the lack of ground truth renders it hard to determine the accuracy of the ML reconstruction. In fact, recent endeavors to determine the precise location of the ML in postmortem dissections concluded that "even applying the most proficient fiber microdissection, the tip of the temporal loop could not be accurately delineated" (Goga and Türe, 2015). Last, the OR travels in part parallel to other white-matter tracts. In particular, it passes parallel to the ILF, and joins the IFOF and the F. Major to form the Sagittal Stratum, making it hard to physically distinguish between them (Catani et al., 2003). It is possible that future high-resolution images and different qMRI parameters will provide additional segmentation power in these regions.

While quantitative MRI methods have become more widely used, they are still not used routinely in research and clinical settings, mostly due to long acquisition times. Furthermore, quantitative T1 mapping is challenging as it must account for instrumental biases and confounds (Boudreau et al., 2017; Curnes et al., 1988). We used a sample of the HCP dataset to demonstrate the ability to optimize the OR tractography results using semi-quantitative MRI. This supports previous studies reporting that the OR is characterized by an increased signal intensity on T1-weighted images and decreased signal intensity on T2-weighted images (Jolesz et al., 1987; Kitajima et al., 1996). This generalizes the applicability of the OR multimodal tractography filtering approach to published datasets, and suggests that it might also be applicable in clinical settings where quantitative MRI measurements are still not commonly available. Nevertheless, we stress that our results are based on data acquired at 3T. As both T1 and T2, as well as their corresponding weighted images, depend on field strength (De Graaf et al., 2006; Stanisz et al., 2005), one should verify that sufficient contrast exists between the OR and adjacent white matter when applying the filtering algorithm at different field strengths.

To conclude, methods for microstructure informed tractography aim

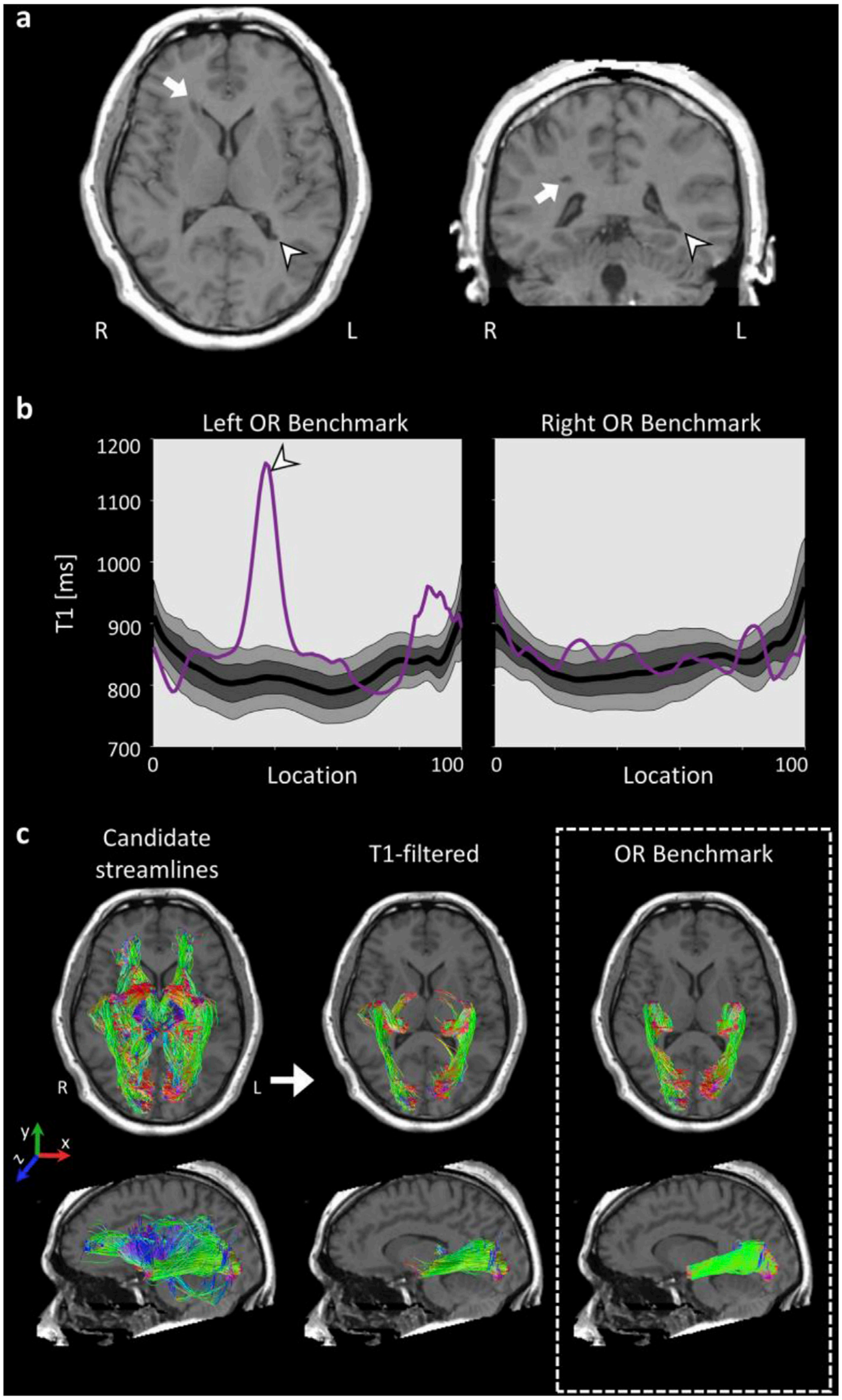


**Fig. 8. T1-filtering in the presence of focal white-matter lesions.** (**a**) T1-weighted axial and sagittal images of the individual with multiple sclerosis. White arrowheads show the same lesion along the OR, near the left lateral ventricle. White arrows indicate two other lesions. (**b**) T1 profiles of the individual with multiple sclerosis (purple) compared with the distribution of measurements from the healthy controls. The lesion is reflected by high T1 values (white arrowhead). (**c**) By ignoring the lesioned voxels when calculating T1-STD and T1-Mdn per streamline, T1-filtering can be applied to the candidate streamline set (left), to obtain a T1-filtered subset (middle) which resembles the OR benchmark (right) in this subject.

at complementing the geometrical aspect of tractography with biophysically meaningful parameters (Daducci et al., 2016, 2015; Girard et al., 2016; Sherbondy et al., 2010, 2008a; Smith et al., 2015) (see Daducci (2016) for review). Such methods, currently based only on diffusion MRI, aim to optimize the accuracy of tractography results, while giving a more complete characterization of white-matter tracts in terms of their microstructural properties (Daducci et al., 2015; Pestilli et al., 2014; Smith et al., 2015). Our findings provide evidence that T1 tract profiles contain valuable microstructural information for optimizing the tractography results in the OR. Importantly, microstructural informed tractography algorithms implicitly assume smoothness in the microstructural signature along white-matter tracts (Daducci et al., 2016). Our results show that in the case of T1 along the OR, this assumption is valid and constructive. We expect that integrative multi-modal approaches for tractography evaluation will become more widely used (Daducci et al., 2016; Wandell, 2016) as more rapid and accurate qMRI methods are developed (Cohen and Polimeni, 2018; Ma et al., 2013) and new acquisition schemes for simultaneously collecting diffusion and relaxometry data are proposed (Benjamini and Basser, 2016; De Santis et al., 2016; Tax et al., 2017).

## Conflicts of interest

The authors declare no conflict of interest in the context of this study.

## Acknowledgements

This work was supported by the NARSAD Young Investigator Grant from the Brain & Behavior Research Foundation and ISF Grant (no. 0399306) awarded to A.A.M., the NSF/SBE-BSF Grants (NSF no. 1551330 and BSF no. 2015608) awarded to A.A.M. and J.D.Y., the National Eye Institute Grants EY018875 and EY015790 awarded to A.M.N, and a seed grant from the Eric Roland Fund for Interdisciplinary Research administered by ELSC, awarded to A.A.M. and R.S.

We thank Brian A. Wandell for data collection, which was supported by the Weston Havens Foundation Grant and the Simons Foundation (Project on Scientific Transparency) Grant. Data were provided in part by the Human Connectome Project, WU-Minn Consortium (Principal Investigators: David Van Essen and Kamil Ugurbil; 1U54MH091657) funded by the 16 NIH Institutes and Centers that support the NIH Blueprint for Neuroscience Research; and by the McDonnell Center for Systems Neuroscience at Washington University. We thank Franco Pestilli and Cesar Caiafa for sharing code and software. Their work was supported by the NSF Grant IIS-1636893 and the NIH Grant ULTTR001108. We thank Christine Tardif and Mallar Chakravarty for sharing data, and Brian A. Wandell, Hiromasa Takemura, Kevin Weiner and Shai Berman, Shir Filo and Batsheva Weisinger for helpful comments on this manuscript.


## Appendix A. Supplementary data

Supplementary data related to this article can be found at https://doi.org/10.1016/j.neuroimage.2018.06.060.

## Appendix B. OR benchmark creation

The validation of any tractography method is difficult due to a lack of ground-truth data regarding the exact spatial extent of the underlying white-matter tracts. Therefore, in order to assess the validity of each tractography-filtering method used in this work, we developed an automated procedure for creating subject-specific benchmark OR bundles. The OR benchmark is a subset of the candidate OR set, but unlike the T1-filtered subset which is the focus of this work, it is filtered using spatial inclusion and exclusion criteria rather than microstructural ones. The benchmark generation process comprises of the following steps (see https://github.com/MezerLab/T1-filtering-OR):

1) Generate 100,000 candidate OR streamlines using ConTrack's probabilistic tractography algorithm, as described in the Methods section. All candidate OR streamlines have endpoints within the thalamus and V1 ROIs.
2) Include only streamlines with endpoints at the LGN. An inclusive LGN is automatically defined based on the thalamus ROI extracted from FreeSurfer: it is defined as a sphere with radius 4 mm, whose center is located at the thalamus' 20% most posterior coordinates, 20% most lateral coordinates, and 10% most inferior coordinates.
3) Eliminate all streamlines crossing the corpus callosum to the contralateral hemisphere.
4) Eliminate all streamlines reaching more than 30 mm inferior of the LGN. Such spurious streamlines often go through the pons and should be discarded.
5) Eliminate streamlines mixing with the callosum Forceps Major. Such spurious streamlines are very common in tractography of the OR. Here we eliminate them using the following 1D histogram classification (Fig. 9):
   5a For every streamline, identify only coordinates extending 20 mm posterior of the LGN, and up to 50% of the total length of the streamline, i.e., before the OR diverges towards its cortical endpoints (Fig. 9, yellow region).
   5b Divide the selected coordinates to 6 evenly spaced bins along the anterior-posterior axis
   5c Select the bin whose distribution of coordinates in the medial-lateral axis is widest (i.e., greatest STD in the x coordinate. Fig. 9, white arrows).
   5d Calculate the minimal-x coordinate of each streamline within the selected bin (Fig. 9).
   5e To classify streamlines as belonging to splenium or OR calculate a histogram of these x coordinates. Identify the boundary between the OR and the splenium as the longest consecutive region with no streamlines along the histogram x-axis (Fig. 9). Keep only the lateral OR streamlines.
6) Eliminate any gross outliers using the standard cleaning procedure of AFQ (Yeatman et al., 2012). Specifically, use a permissive threshold to discard any streamlines whose length is more than 4 standard deviations above the mean streamline length.

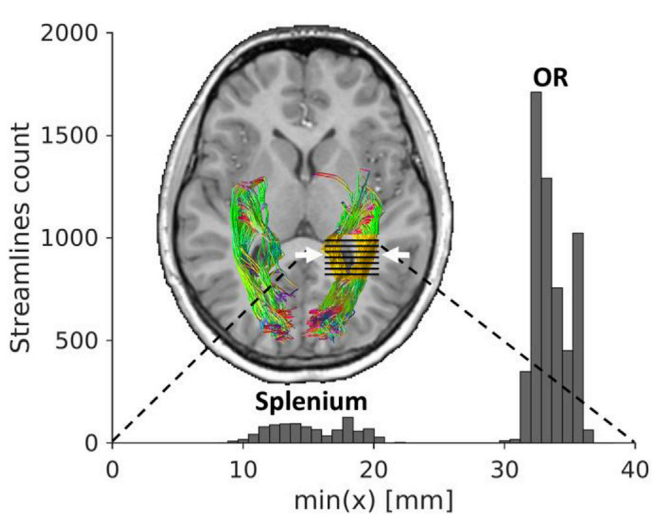


**Fig. 9. Histogram classification for eliminating the spurious splenium streamlines.** Only the segment of the streamlines posterior to the LGN, and up to 50% of the total streamline length are considered (yellow). This segment is divided to 6 bins along the posterior-anterior axis (y). The bin with the widest distribution in the

lateral-medial (x) axis is used for classification. In this bin, a histogram of the minimal-x coordinates is calculated. Dashed lines mark the range of x values used in the histogram plot. This histogram is typically bi-modal, reflecting the fact that the lateral ventricle separates the medial splenium from the lateral OR. Only streamline in the lateral group are retained in the final benchmark.

See Fig. 5d and Supplementary Figs. 5-9 for examples of the resulting OR benchmark.

## References


Alexander, D.C., Dyrby, T.B., Nilsson, M., Zhang, H., 2017. Imaging brain microstructure with diffusion MRI: practicality and applications. NMR Biomed. https://doi.org/10.1002/nbm.3841.

Avants, B., Tustison, N., Song, G., 2009. Advanced normalization tools (ANTs). Insight J 2, 1–35.

Barral, J.K., Gudmundson, E., Stikov, N., Etezadi-amoli, M., Stoica, P., Nishimura, D.G., 2010. A robust methodology for in vivo T1 mapping. Magn. Reson. Med. 64 (4), 1057–1067.

Bastiani, M., Shah, N.J., Goebel, R., Roebroeck, A., 2012. Human cortical connectome reconstruction from diffusion weighted MRI: the effect of tractography algorithm. Neuroimage 62, 1732–1749.

Benjamin, C.F.A., Singh, J.M., Prabhu, S.P., Warfield, S.K., 2014. Optimization of tractography of the optic radiations. Hum. Brain Mapp. 35, 683–697.

Benjamini, D., Basser, P.J., 2016. Use of marginal distributions constrained optimization (MADCO) for accelerated 2D MRI relaxometry and diffusometry. J. Magn.Reson. 271, 40–45.

Berman, S., West, K.L., Does, M.D., Yeatman, J.D., Mezer, A.A., 2017. Evaluating g-ratio weighted changes in the corpus callosum as a function of age and sex. Neuroimage.

Boudreau, M., Tardif, C.L., Stikov, N., Sled, J.G., Lee, W., Pike, G.B., 2017. B1 mapping for bias-correction in quantitative T1 imaging of the brain at 3T using standard pulse sequences. J. Mag. Reson. Imag. 46 (6), 1673–1682.

Bürgel, U., Schormann, T., Schleicher, A., Zilles, K., 1999. Mapping of histologically identified long fiber tracts in human cerebral hemispheres to the MRI volume of a reference brain: position and spatial variability of the optic radiation. Neuroimage 10, 489–499.

Bürgel, U., Amunts, K., Hoemke, L., Mohlberg, H., Gilsbach, J.M., Zilles, K., 2006. White matter fiber tracts of the human brain: three-dimensional mapping at microscopic resolution, topography and intersubject variability. Neuroimage 29, 1092–1105.

Caiafa, C.F., Pestilli, F., 2017. Multidimensional encoding of brain connectomes. Sci. Rep. 7 (1), 11491.

Catani, M., Thiebaut de Schotten, M., 2008. A diffusion tensor imaging tractography atlas for virtual in vivo dissections. Cortex 44, 1105–1132.

Catani, M., Jones, D.K., Donato, R., Ffytche, D.H., 2003. Occipito-temporal connections in the human brain. Brain 126, 2093–2107.

Chamberland, M., Scherrer, B., Prabhu, S.P., Madsen, J., Fortin, D., Whittingstall, K., Descoteaux, M., Warfield, S.K., 2016. Active delineation of Meyer's loop using oriented priors through MAGNEtic tractography (MAGNET). Hum. Brain Mapp. 38 (1), 509–527.

Chenevert, T.L., Brunberg, J.A., Pipe, J.G., 1990. Anisotropic diffusion in human white matter: demonstration with MR techniques in vivo. Radiology 177, 401–405.

Clatworthy, P.L., Williams, G.B., Acosta-Cabronero, J., Jones, S.P., Harding, S.G., Johansen-Berg, H., Baron, J.C., 2010. Probabilistic tractography of the optic radiations - an automated method and anatomical validation. Neuroimage 49, 2001–2012.

Cohen, O., Polimeni, J.R., 2018. Optimized inversion-time schedules for quantitative T1 measurements based on high-resolution multi-inversion EPI. Magn. Reson. Med. 79 (4), 2101–2112.

Curnes, J.T., Burger, P.C., Djang, W.T., Boyko, O.B., 1988. MR imaging of compact white matter pathways. AJNR. Am. J. Neuroradiol. 9, 1061–1068.

Daducci, A., Dal Palu, A., Lemkaddem, A., Thiran, J.P., 2015. COMMIT: convex optimization modeling for microstructure informed tractography. IEEE Trans. Med. Imag. 34, 246–257.

Daducci, A., Dal Palú, A., Descoteaux, M., Thiran, J.-P., 2016. Microstructure informed tractography: pitfalls and open challenges. Front. Neurosci. 10, 1–13.

Dayan, M., Munoz, M., Jentschke, S., Chadwick, M.J., Cooper, J.M., Riney, K., Vargha-Khadem, F., Clark, C.A., 2015. Optic radiation structure and anatomy in the normally developing brain determined using diffusion MRI and tractography. Brain Struct. Funct. 220, 291–306.

De Graaf, R.A., Brown, P.B., Mcintyre, S., Nixon, T.W., Behar, K.L., Rothman, D.L., 2006. High magnetic field water and metabolite proton T1 and T2 relaxation in rat brain in vivo. Magn. Reson. Med. 56, 386–394.

De Santis, S., Assaf, Y., Jeurissen, B., Jones, D.K., Roebroeck, A., 2016. T1 relaxometry of crossing fibres in the human brain. Neuroimage 141, 133–142.

Duan, Y., Norcia, A.M., Yeatman, J.D., Mezer, A., 2015. The structural properties of major white matter tracts in strabismic amblyopia. Invest. Ophthalmol. Vis. Sci. 56, 5152–5160.

Ebeling, U., Reulen, H.J., 1988. Neurosurgical topography of the optic radiation in the temporal lobe. Acta Neurochir. 92, 29–36.

Feinberg, D.A., Moeller, S., Smith, S.M., Auerbach, E., Ramanna, S., Glasser, M.F., Miller, K.L., Ugurbil, K., Yacoub, E., 2010. Multiplexed echo planar imaging for sub-second whole brain FMRI and fast diffusion imaging. PLoS One 5 (12) e15710.

Ferguson, J.S., 1905. Normal histology and Microscopical Anatomy. D. Appleton and Company.

Fischl, B., 2012. FreeSurfer. Neuroimage 62, 774–781.

Frank, L.R., 2001. Anisotropy in high angular resolution diffusion-weighted MRI. Magn. Reson. Med. 45, 935–939.

Girard, G., Whittingstall, K., Deriche, R., Descoteaux, M., 2014. Towards quantitative connectivity analysis: reducing tractography biases. Neuroimage 98, 266–278.

Girard, G., Fick, R., Descoteaux, M., Deriche, R., 2016. AxTract: microstructure-driven tractography based on the ensemble average propagator. In: International Conference on Information Processing in Medical Imaging, pp. 675–686.

Glasser, M.F., Van Essen, D.C., 2011. Mapping human cortical areas in vivo based on myelin content as revealed by T1- and T2-weighted MRI. J. Neurosci. 31, 11597–11616.

Goga, C., Türe, U., 2015. The anatomy of Meyer's loop revisited: changing the anatomical paradigm of the temporal loop based on evidence from fiber microdissection. J. Neurosurg. 122, 1–10.

Hoon, A.H.J., Stashinko, E.E., Nagae, L.M., Lin, D.D., Keller, J., Bastian, A., Campbell, M.L., Levery, E., Mori, S., Johnston, M.V., 2009. Sensory and motor deficits in children with cerebral palsy born preterm correlate with diffusion tensor imaging abnormalities in thalamocortical pathways. Dev. Med. Child Neurol. 51, 697–704.

Jbabdi, S., Johansen-Berg, H., 2011. Tractography: where do we go from here? Brain Connect. 1, 169–183.

Jbabdi, S., Sotiropoulos, S.N., Haber, S.N., Van Essen, D.C., Behrens, T.E., 2015. Measuring macroscopic brain connections in vivo. Nat. Neurosci. 18, 1546–1555.

Jolesz, F.A., Polak, J.F., Adams, D.F., Ruenzel, P.W., 1987. Myelinated and nonmyelinated nerves: comparison of proton MR properties. Radiology 164, 89–91.

Jones, D.K., Horsfield, M.A., Simmons, A., 1999. Optimal strategies for measuring diffusion in anisotropic systems by magnetic resonance imaging. Magn. Reson. Med. 42, 515–525.

Kammen, A., Law, M., Tjan, B.S., Toga, A.W., Shi, Y., 2016. Automated retinofugal visual pathway reconstruction with multi-shell HARDI and FOD-based analysis. Neuroimage 125, 767–779.

Kaushik, M., Graham, S.L., Wang, C., Klistorner, A., 2014. A topographical relationship between visual field defects and optic radiation changes in glaucoma. Investig. Opthalmology Vis. Sci. 55 (5770).

Kier, E.L., Staib, L.H., Davis, L.M., Bronen, R.A., 2004. MR imaging of the temporal stem: anatomic dissection tractography of the uncinate Fasciculus, inferior occipitofrontal Fasciculus, and Meyer's loop of the optic radiation. AJNR. Am. J. Neuroradiol 25, 677–691.

Kitajima, M., Korogi, Y., Takahashi, M., Eto, K., 1996. MR signal intensity of the optic radiation. Am. J. Neuroradiol. 17, 1379–1383.

Knösche, T.R., Anwander, A., Liptrot, M., Dyrby, T.B., 2015. Validation of tractography: comparison with manganese tracing. Hum. Brain Mapp. 36, 4116–4134.

Li, L., Rilling, J.K., Preuss, T.M., Glasser, M.F., Hu, X., 2012. The effects of connection reconstruction method on the interregional connectivity of brain networks via diffusion tractography. Hum. Brain Mapp. 1894–1913.

Lilja, Y., Nilsson, D.T., 2015. Strengths and limitations of tractography methods to identify the optic radiation for epilepsy surgery. Quant. Imag. Med. Surg. 5, 288–299.

Lilja, Y., Ljungberg, M., Starck, G., Malmgren, K., Rydenhag, B., Nilsson, D.T., 2014. Visualizing Meyer's loop: a comparison of deterministic and probabilistic tractography. Epilepsy Res. 108, 481–490.

Lim, J.C., Phal, P.M., Desmond, P.M., Nichols, A.D., Kokkinos, C., Danesh-Meyer, H.V., Kaye, A.H., Moffat, B.A., 2015. Probabilistic MRI tractography of the optic radiation using constrained spherical deconvolution: a feasibility study. PLoS One 10 e0118948.

Lutti, A., Dick, F., Sereno, M.I., Weiskopf, N., 2014. Using high-resolution quantitative mapping of R1 as an index of cortical myelination. Neuroimage 93, 176–188.

Ma, D., Gulani, V., Seiberlich, N., Liu, K., Sunshine, J.L., Duerk, J.L., Griswold, M.A., 2013. Magnetic resonance fingerprinting. Nature 495, 187–192.

Maier-Hein, K.H., Neher, P.F., Houde, J.-C., Côté, M.-A., Garyfallidis, E., Zhong, J., Chamberland, M., Yeh, F.-C., Lin, Y.-C., Ji, Q., Reddick, W.E., Glass, J.O., Chen, D.Q., Feng, Y., Gao, C., Wu, Y., Ma, J., Renjie, H., Li, Q., Westin, C.-F., Deslauriers-Gauthier, S., González, J.O.O., Paquette, M., St-Jean, S., Girard, G., Rheault, F., Sidhu, J., Tax, C.M.W., Guo, F., Mesri, H.Y., Dávid, S., Froeling, M., Heemskerk, A.M., Leemans, A., Boré, A., Pinsard, B., Bedetti, C., Desrosiers, M., Brambati, S., Doyon, J., Sarica, A., Vasta, R., Cerasa, A., Quattrone, A., Yeatman, J., Khan, A.R., Hodges, W., Alexander, S., Romascano, D., Barakovic, M., Auría, A., Esteban, O., Lemkaddem, A., Thiran, J.P., Cetingul, H.E., Odry, B.L., Mailhe, B., Nadar, M.S., Pizzagalli, F., Prasad, G., Villalon-Reina, J.E., Galvis, J., Thompson, P.M., Requejo, F.D.S., Laguna, P.L., Lacerda, L.M., Barrett, R., Dell'Acqua, F., Catani, M., Petit, L., Caruyer, E., Daducci, A., Dyrby, T.B., Holland-Letz, T., Hilgetag, C.C., Stieltjes, B., Descoteaux, M., 2017. The challenge of mapping the human connectome based on diffusion tractography. Nat. Commun. 8 (1349).

Mangin, J.F., Poupon, C., Cointepas, Y., Rivière, D., Papadopoulos-Orfanos, D., Clark, C.A., Régis, J., Le Bihan, D., 2002. A framework based on spin glass models for the inference of anatomical connectivity from diffusion-weighted MR data - a technical review. NMR Biomed. 15, 481–492.

Martínez-heras, E., Varriano, F., Pr, V., Laredo, C., 2015. Improved framework for tractography reconstruction of the optic radiation. PLoS One 1–16.

Mezer, A., Yeatman, J.D., Stikov, N., Kay, K.N., Cho, N.-J., Dougherty, R.F., Perry, M.L., Parvizi, J., Hua, L.H., Butts-Pauly, K., Wandell, B.A., 2013. Quantifying the local

tissue volume and composition in individual brains with magnetic resonance imaging. Nat. Med. 19, 1667–1672.
Mezer, A., Rokem, A., Berman, S., Hastie, T., Wandell, B.A., 2016. Evaluating quantitative proton-density-mapping methods. Hum. Brain Mapp. 37 (10), 3623–3635.
Moeller, S., Yacoub, E., Olman, C.A., Auerbach, E., Strupp, J., Harel, N., Uğurbil, K., 2010. Multiband multislice GE-EPI at 7 tesla, with 16-fold acceleration using partial parallel imaging with application to high spatial and temporal whole-brain fMRI. Magn. Reson. Med. 63, 1144–1153.
Ogawa, S., Takemura, H., Horiguchi, H., Terao, M., Haji, T., Pestilli, F., Yeatman, J.D., Tsuneoka, H., Wandell, B.A., Masuda, Y., 2014. White matter consequences of retinal receptor and ganglion cell damage. Invest. Ophthalmol. Vis. Sci. 55, 6976–6986.
Ozarslan, E., Koay, C.G., Shepherd, T.M., Komlosh, M.E., İrfanoğlu, M.O., Pierpaoli, C., Basser, P.J., 2013. Mean apparent propagator (MAP) MRI: a novel diffusion imaging method for mapping tissue microstructure. Neuroimage 78, 16–32.
Pestilli, F., Yeatman, J.D., Rokem, A., Kay, K.N., Wandell, B.A., 2014. Evaluation and statistical inference for human connectomes. Nat. Methods 11 (10), 1058–1063.
Portegies, J.M., Fick, R.H.J., Sanguinetti, G.R., Meesters, S.P.L., Girard, G., Duits, R., 2015. Improving fiber alignment in HARDI by combining contextual PDE flow with constrained sphaerical deconvolution. PLoS One 10 (10), 1–33.
Reich, D.S., Smith, S.A., Gordon-Lipkin, E.M., Ozturk, A., Caffo, B.S., Balcer, L.J., Calabresi, P.A., 2009. Damage to the optic radiation in multiple sclerosis is associated with retinal injury and visual disability. Arch. Neurol. 66, 998–1006.
Renauld, E., Descoteaux, M., Bernier, M., Garyfallidis, E., Whittingstall, K., 2016. Semi-automatic segmentation of optic radiations and LGN, and their relationship to EEG alpha waves. PLoS One 11 (7) e0156436.
Rokem, A., Yeatman, J.D., Pestilli, F., Kay, K.N., Mezer, A., van der Walt, S., Wandell, B.A., 2015. Evaluating the accuracy of diffusion MRI models in white matter. PLoS One 10 (4) e0123272.
Rushe, T., Nosarti, C., Hack, M., Murray, R.M., 2010. Neurodevelopmental Outcomes of Preterm Birth: from Childhood to Adult Life: Language Development. Cambridge University Press.
Sarubbo, S., De Benedictis, A., Milani, P., Paradiso, B., Barbareschi, M., Rozzanigo, U., Colarusso, E., Tugnoli, V., Farneti, M., Granieri, E., Duffau, H., Chioffi, F., 2015. The course and the anatomo-functional relationships of the optic radiation: a combined study with "post mortem" dissections and "in vivo" direct electrical mapping. J. Anat. 226, 47–59.
Setsompop, K., Gagoski, B.A., Polimeni, J.R., Witzel, T., Wedeen, V.J., Wald, L.L., 2012. Blipped-controlled aliasing in parallel imaging for simultaneous multislice echo planar imaging with reduced g-factor penalty. Magn. Reson. Med. 67, 1210–1224.
Sherbondy, A.J., Dougherty, R.F., Ben-Shachar, M., Napel, S., Wandell, B.A., 2008a. ConTrack: finding the most likely pathways between brain regions using diffusion tractography. J. Vis. 8, 15.1-16.
Sherbondy, A.J., Dougherty, R.F., Wandell, B.A., 2008b. Identifying the human optic radiation using diffusion imaging and fiber. tractography 8, 1–11.
Sherbondy, A.J., Rowe, M.C., Alexander, D.C., 2010. MicroTrack: an algorithm for concurrent projectome and microstructure estimation. In: Jiang, T., Navab, N., Pluim, J.P.W., Viergever, M.A. (Eds.), Medical Image Computing and Computer-Assisted Intervention – MICCAI 2010, MICCAI 2010. Lecture Notes in Computer Science, vol. 6361. Springer, Berlin, Heidelberg.
Smith, R.E., Tournier, J.D., Calamante, F., Connelly, A., 2012. Anatomically-constrained tractography: improved diffusion MRI streamlines tractography through effective use of anatomical information. Neuroimage 62, 1924–1938.
Smith, R.E., Tournier, J.D., Calamante, F., Connelly, A., 2015. SIFT2: enabling dense quantitative assessment of brain white matter connectivity using streamlines tractography. Neuroimage 119, 338–351.
Sotiropoulos, S.N., Moeller, S., Jbabdi, S., Xu, J., Andersson, J.L., Auerbach, E.J., Yacoub, E., Feinberg, D., Setsompop, K., Wald, L.L., Behrens, T.E.J., Ugurbil, K., Lenglet, C., 2013. Effects of image reconstruction on fiber orientation mapping from multichannel diffusion MRI: reducing the noise floor using SENSE. Magn. Reson. Med. 70, 1682–1689.
Stanisz, G.J., Odrobina, E.E., Pun, J., Escaravage, M., Graham, S.J., Bronskill, M.J., Henkelman, R.M., 2005. T1, T2 relaxation and magnetization transfer in tissue at 3T. Magn. Reson. Med. 54 (3), 507–512. https://www.ncbi.nlm.nih.gov/pubmed/16086319.
Stejskal, E.O., Tanner, J.E., 1965. Spin diffusion measurements: spin echoes in the presence of a time-dependant field gradient. J. Chem. Phys. 42 (1), 288–292.
Stieglitz, L.H., Lüdemann, W.O., Giordano, M., Raabe, A., Fahlbusch, R., Samii, M., 2011. Optic radiation fiber tracking using anteriorly angulated diffusion tensor imaging: a tested algorithm for quick application. Neurosurgery 68, 1239–1251.
Stüber, C., Morawski, M., Schäfer, A., Labadie, C., Wähnert, M., Leuze, C., Streicher, M., Barapatre, N., Reimann, K., Geyer, S., Spemann, D., Turner, R., 2014. Myelin and iron concentration in the human brain: a quantitative study of MRI contrast. Neuroimage 93 (Pt 1), 95–106.
Takemura, H., Caiafa, C.F., Wandell, B.A., Pestilli, F., 2016. Ensemble tractography. PLoS Comput. Biol. 12 e1004692.
Tax, C.M.W., Rudrapatna, U.S., Witzel, T., Jones, D.K., 2017. Disentangling in two dimensions in the living human brain: feasbilty of relaxometry-diffusometry using ultra-strong gradients. In: Proceedings of the 25th Annual International Society of Magnetic Resonance in Medicine (ISMRM) Conference.
Thomas, C., Ye, F.Q., İrfanoğlu, M.O., Modi, P., Saleem, K.S., Leopold, D.A., Pierpaoli, C., 2014. Anatomical accuracy of brain connections derived from diffusion MRI tractography is inherently limited. Proc. Natl. Acad. Sci. Unit. States Am. 111, 16574–16579.
Tournier, J.D., Calamante, F., Connelly, A., 2007. Robust determination of the fibre orientation distribution in diffusion MRI: non-negativity constrained super-resolved spherical deconvolution. Neuroimage 35, 1459–1472.
Tournier, J.D., Calamante, F., Connelly, A., 2012. MRtrix: diffusion tractography in crossing fiber regions. Int. J. Imaging Syst. Technol. 22, 53–66.
Tuch, D.S., Reese, T.G., Wiegell, M.R., Wedeen, V.J., 2003. Diffusion MRI of Complex Neural Architecture, 40, pp. 885–895.
Tustison, N.J., Avants, B.B., Cook, P.A., Yuanjie Zheng, Y., Egan, A., Yushkevich, P.A., Gee, J.C., 2010. N4ITK: improved N3 bias correction. IEEE Trans. Med. Imag. 29, 1310–1320.
Tustison, N.J., Cook, P.A., Klein, A., Song, G., Das, S.R., Duda, J.T., Kandel, B.M., Strien, N. Van, Stone, J.R., Gee, J.C., Avants, B.B., 2014. Large-scale evaluation of ANTs and FreeSurfer cortical thickness measurements. Neuroimage 99, 166–179.
Van Essen, D.C., Ugurbil, K., Auerbach, E., Barch, D., Behrens, T.E.J., Bucholz, R., Chang, A., Chen, L., Corbetta, M., Curtiss, S.W., Della Penna, S., Feinberg, D., Glasser, M.F., Harel, N., Heath, A.C., Larson-Prior, L., Marcus, D., Michalareas, G., Moeller, S., Oostenveld, R., Petersen, S.E., Prior, F., Schlaggar, B.L., Smith, S.M., Snyder, A.Z., Xu, J., Yacoub, E., WU-Minn HCP Consortium, 2012. The Human Connectome Project: a data acquisition perspective. Neuroimage 62, 2222–2231.
Wakana, S., Jiang, H., Nagae-Poetscher, L.M., van Zijl, P.C.M., Mori, S., 2004. Fiber tract-based atlas of human white matter anatomy. Radiology 230, 77–87.
Wandell, B.A., 2016. Clarifying human white matter. Annu. Rev. Neurosci. 39, 103–128.
Williams, T., Gluhbegoric, N., Jew, J., 1997. The Human Brain: Dissections of the Real Brain. Virtual Hospital, University of Iowa online: http://163.178.103.176/Temas/Temab2N/APortal/FisoNerCG/LaUII/Neuro/BrainAn/Introduction.html.
Winston, G.P., Daga, P., White, M.J., Micallef, C., Miserocchi, A., Mancini, L., Modat, M., Stretton, J., Sidhu, M.K., Symms, M.R., Lythgoe, D.J., Thornton, J., Yousry, T.A., Ourselin, S., Duncan, J.S., McEvoy, A.W., 2014. Preventing visual field deficits from neurosurgery. Neurology 83, 604–611.
Xie, S., Gong, G.L., Xiao, J.X.I., Ye, J.T., Liu, H.H., Gan, X.L., Jiang, Z.T., Jiang, X.X., 2007. Underdevelopment of optic radiation in children with amblyopia: a tractography study. Am. J. Ophthalmol. 143, 642–646.
Yeatman, J.D., Wandell, B.A., Mezer, A.A., 2014. Lifespan maturation and degeneration of human brain white matter. Nat. Commun. 5 (4932).
Yeatman, J.D., Dougherty, R.F., Myall, N.J., Wandell, B.A., Feldman, H.M., 2012. Tract profiles of white matter properties: automating fiber-tract quantification. PLoS One 7 e49790.
Yogarajah, M., Focke, N.K., Bonelli, S., Cercignani, M., Acheson, J., Parker, G.J.M., Alexander, D.C., McEvoy, A.W., Symms, M.R., Koepp, M.J., Duncan, J.S., 2009. Defining Meyer's loop-temporal lobe resections, visual field deficits and diffusion tensor tractography. Brain 132, 1656–1668.
Youden, W.J., 1950. Index for rating diagnostic tests. Cancer 3, 32–35.
Zalesky, A., Fornito, A., Cocchi, L., Gollo, L.L., van den Heuvel, M.P., Breakspear, M., 2016. Connectome sensitivity or specificity: which is more important? Neuroimage 142, 407–420.